


# COST-EFFECTIVE CFD REPRODUCTION OF DPW-7 CASE 2A FOR CRM TRANSONIC PITCHING-MOMENT PREDICTION AND ADAPTIVE-REFINEMENT ASSESSMENT

Gustavo Colombi Ribolla[1], Lourenço Junqueira Franco Meirelles[1], Luis Filippe Silva Gomes[1], Melina Belli Stergiou[1], Rodrigo Milare Granzoto[2], Paulo Bufacchi[1]

[1]Insper, Rua Quatá 300, Vila Olímpia, São Paulo, SP 04546-042, Brazil
[2]Embraer S.A., Av. Brig. Faria Lima 2170, Putim, São José dos Campos, SP 12227-901, Brazil

## Abstract

Accurate transonic aerodynamic prediction remains difficult in aircraft design, particularly for pitching moment, which is highly sensitive to shock location, shock motion, and shock-induced separation. This paper reproduces Case 2a of the seventh AIAA Drag Prediction Workshop for NASA's Common Research Model wing-body configuration at Mach 0.85 and a Reynolds number of 20 million. The study uses a cost-constrained baseline mesh of approximately 4.69 million cells to perform an angle-of-attack sweep and to assess the trade-off between computational cost and aerodynamic fidelity. Results are compared with wind-tunnel measurements, workshop submissions, and higher-resolution reference simulations. The reduced mesh captures the main lift and drag trends, but it shows larger errors in pitching moment and predicts the pitch-break onset slightly early. A vorticity-based adaptive mesh refinement test is also evaluated at alpha = 4.00 degrees. Localized refinement slightly reduces drag, but it does not improve lift or pitching moment, indicating that refinement criteria based only on vorticity are insufficient for moment-sensitive transonic flows. The results show that low-cost meshes can support exploratory assessments, but reliable pitching-moment prediction requires refinement targeted to shock, separation and near-wall regions that directly control chordwise pressure loading.

**Keywords:** CFD; Common Research Model; DPW-7; pitching moment; adaptive mesh refinement.

## 1. Introduction

Accurate prediction of transonic aerodynamic performance remains a central challenge in aircraft design. In this regime, subsonic and supersonic flow regions coexist around the aircraft, leading to shock formation, shock motion, and shock-boundary-layer interaction. These mechanisms strongly affect lift, drag and pitching moment, with direct implications for stability, control, and aerodynamic efficiency [4,11,12].

Among these quantities, the pitching moment is particularly sensitive to chordwise pressure loading. Small changes in shock position or in the extent of shock-induced separation can shift the aerodynamic loading and produce nonlinear variations in the pitching-moment curve. In transonic flows, this behavior is commonly associated with pitch break, which appears as an abrupt change in the slope of the pitching-moment curve as the angle of attack increases. Predicting the onset and progression of this behavior is therefore a demanding test for computational fluid dynamics (CFD) methods [4,11,12].

Benchmarking initiatives such as the American Institute of Aeronautics and Astronautics Drag Prediction Workshop provide standardized cases for assessing numerical methods under representative aerodynamic conditions [1,2,18]. The seventh Drag Prediction Workshop (DPW-7) uses NASA's Common Research Model as a reference configuration and provides experimental data and participant submissions that support consistent comparison of numerical approaches, turbulence models and mesh strategies [1,9,19]. Case 2a considers the Common Research Model wing-body

https://doi.org/10.71945/icas2026_0953

configuration at Mach 0.85 and a Reynolds number of 20 million, with an angle-of-attack sweep designed to assess nonlinear aerodynamic behavior and pitching-moment prediction [1,7,18].
In practical CFD workflows, predictive accuracy must be balanced against computational cost. High-resolution meshes can improve the representation of shocks, separation and near-wall flow, but they require substantial memory, long runtimes and significant computational resources. This trade-off is especially relevant in preliminary design, parametric studies and academic projects, where multiple operating conditions must be evaluated under constrained resources [5,6,8,10,18].
Localized mesh refinement offers one possible route to improve this balance. Instead of refining the entire domain uniformly, additional cells can be concentrated in regions where the flow is expected to be complex and relevant to the aerodynamic quantity of interest. Adaptive mesh refinement (AMR) follows this principle, but its effectiveness depends on the refinement indicator and on whether the refined regions control the target aerodynamic response [20,21,22,23,24].
This work reproduces DPW-7 Case 2a and investigates how mesh resolution and AMR affect the prediction of transonic aerodynamic behavior and computational cost. A reduced baseline mesh with approximately 4.69 million cells is used for the complete angle-of-attack sweep, and the results are compared with wind-tunnel data, DPW-7 submissions and higher-resolution simulations [5,6,7,8,10,18]. Attention is given to pitching moment and pitch-break prediction. A vorticity-based AMR test at AoA = 4.00 degrees is then used to assess whether localized refinement improves the prediction of integral aerodynamic coefficients in a moment-sensitive transonic flow.

## 2. Geometry and Domain Definition

The meshes provided by the DPW-7 workshop are highly refined and contain a very large number of cells, leading to substantial computational cost and long runtimes [1,3,18]. Given the resource limits of the present study, an alternative cost-constrained strategy was adopted to obtain physically consistent aerodynamic trends with a substantially smaller grid.
The NASA Common Research Model geometry available from the official DPW-7 repository was used for each angle of attack considered [1,9,19]. The geometries include the aeroelastic deformations measured in wind-tunnel tests, maintaining consistency between the numerical models and the experimental reference data [7,18].
After the geometry was imported into the CFD software, it was prepared according to the requirements of DPW-7 Case 2a. Because this case considers the wing-body configuration, the horizontal tail was removed from the original model, leaving a configuration focused on the main lifting surfaces and fuselage [1,18].
The computational domain was then generated around the processed geometry. A hemispherical far-field domain was adopted, following Siemens external-aerodynamics guidance and remaining consistent with domain strategies reported in DPW-7-related studies [5,6,8,10,14].
The wing mean aerodynamic chord was used as the reference length for the domain size. The far-field radius was set to 100 mean aerodynamic chords, corresponding to approximately 700 m. This extent was selected to limit far-field boundary influence while keeping the simulations computationally feasible [13,14].
To reduce computational cost, symmetry was imposed on the aircraft center plane. The aircraft surfaces were treated as no-slip walls, the external boundaries were defined as freestream boundaries, and the domain cutting plane was prescribed as a symmetry plane [13,14].
After defining the computational domain and the boundary conditions, the computational mesh used in the simulations was generated.

## 3. Mesh Configuration

Mesh generation was a central step in the proposed cost-constrained workflow. The objective was to retain sufficient resolution in the relevant aerodynamic regions while keeping the total cell count low enough for a complete angle-of-attack sweep.
The mesh was generated with the Automated Mesh feature, combining meshing tools appropriate for the transonic wing-body configuration [13,15]. The Tetrahedral Mesher discretized the main flow domain with unstructured tetrahedral cells, providing flexibility for the wing-body geometry, while the

Prism Layer Mesher generated near-wall prismatic layers to improve boundary-layer resolution and control the dimensionless wall distance y+ [13,15,16]. The Surface Remesher was used to improve surface triangulation, preserve geometric features, and support smooth prism-layer growth [13].
The use of prism layers was particularly important to capture near-wall viscous effects, while tetrahedral elements allowed reduction of the overall computational cost of the mesh [13,15,16].
To ensure consistency across the different angles of attack and to enable future comparisons between cases with and without adaptive refinement, the same mesh configuration was applied to all simulations. The adopted mesh used a base size of 5 m, 65 prism layers, a first-layer thickness of $3.051\times10^{-6}$ m, a total prism-layer thickness of 0.612 m, a surface growth rate of 1.2, a volume growth rate of 1.2, and a surface-curvature resolution of 144 points per circle.
With this setup, the meshes contained approximately 4.7 million cells, corresponding to a reduction of about 97% relative to the official DPW-7 workshop meshes [1,3,18]. Despite this reduction, the mesh retained smooth transitions between prism layers and tetrahedral cells and provided adequate resolution of the main aerodynamic regions for the exploratory objectives of the study.
The present validation emphasizes comparison with wind-tunnel data, DPW-7 submissions, and higher-resolution reference simulations [5,6,7,8,10,18]. A limitation of the present study is that detailed mesh-quality indicators, such as near-wall resolution, skewness, face validity, minimum volume and orthogonality metrics, were not included in the present comparison.

## 4. Adaptive Mesh Refinement (AMR)

Additional settings were implemented to apply Adaptive Mesh Refinement to selected simulations.
AMR was used to increase mesh resolution only in regions identified as dynamically relevant, avoiding uniform refinement of the full domain and preserving the low-cost objective of the study [20,21,22,23,24].
Vorticity magnitude was selected as the refinement indicator. This criterion identifies shear layers, separation regions, wake structures and vortical structures near the wing [13]. Although these features can affect aerodynamic loads, vorticity alone does not necessarily target shock position, shock-foot structure or near-wall pressure gradients, which are critical for pitching-moment prediction in transonic flows [20,21,22,23].
These considerations are important because the pitching moment is controlled by the chordwise pressure distribution. Refinement criteria must therefore be aligned with the physical mechanisms that influence the aerodynamic coefficient being evaluated [20,21,22,23,24].
Refinement cycles were executed automatically during the solution iterations, with predefined limits imposed to avoid excessive mesh growth. The adaptive refinement procedure used vorticity magnitude as the refinement criterion, with a minimum threshold of 0.2, a maximum threshold of 25, a minimum cell size of $1.0\times10^{-4}$ m, and a maximum refinement level of 2 [13].
Cells above the prescribed vorticity threshold were flagged for refinement during the solution process.
To limit cell-count growth and preserve the low-cost objective, AMR was not applied to prism-layer cells. Preliminary tests indicated that refinement in the boundary-layer mesh caused excessive cell growth without proportional improvement in the integral aerodynamic coefficients.

## 5. Numerical Setup

The numerical setup followed the DPW-7 Case 2a conditions and Siemens external-aerodynamics guidance, with selected solver controls adjusted to improve robustness for the transonic flow regime [1,13,14,15].
The Courant-Friedrichs-Lewy number was bounded between 0.5 and 50, providing additional stability during the initial iterations while allowing faster convergence later in the solution. The under-relaxation factors of the Spalart-Allmaras turbulence model were also reduced to improve robustness in regions with strong pressure gradients and shock waves [13,15,16].
An Algebraic Multigrid solver convergence tolerance of 0.001 was adopted to impose tighter residual control during the iterative process [13,15]. These settings were selected to balance numerical stability, convergence rate and solution robustness while remaining close to the recommended setup for this

class of external-aerodynamics simulations [14,15].
The initial and boundary conditions adopted in the simulations followed the specifications of DPW-7 Case 2a, with a Mach number of 0.85, a Reynolds number of 20 million, and a freestream static temperature of 116.48 K [1,7,18]. The freestream velocity was calculated from the Mach number and the local speed of sound, as shown in Equation 1 [4].

$$V_\infty = M_\infty \sqrt{\gamma R T_\infty} \tag{1}$$

Using γ = 1.4, R = 287.05 J kg$^{-1}$ K$^{-1}$, T∞ = 116.48 K and M∞ = 0.85 gives U∞ approximately 184 m s$^{-1}$. For each angle of attack α, the Cartesian velocity components were prescribed as Ux = U∞ cos(α) and Uy = U∞ sin(α), following the adopted coordinate convention.
The same incidence was imposed at the freestream boundary through a direction vector consistent with the prescribed angle of attack, ensuring that the inflow direction and the aerodynamic configuration were matched for each simulation [13,14,15].
Static pressure, density, and dynamic viscosity were taken from the Embraer reference simulations used for comparison, maintaining consistency across datasets.
The physical models, turbulence closure, wall treatment, solver type, discretization schemes, convergence criteria, and boundary conditions are summarized in Table 1.

Table 1 – Initial conditions and setup parameters.

| Physical Modeling | |
|---|---|
| **Parameter** | **Value / Choice** |
| **Fluid** | Ideal gas |
| **Solver** | Coupled Flow |
| **Discretization** | MUSCL 3rd order |
| **Inviscid flux** | AUSM+ |
| **Turbulence** | Spalart-Allmaras |
| **Wall treatment** | All y+ wall treatment |
| **Reference Values** | |
| **Parameter** | **Value / Choice** |
| **Static pressure (p)** | 4194 Pa |
| **Initial Conditions** | |
| **Parameter** | **Value / Choice** |
| **Static temperature (T)** | 116.48 K |
| **Velocity – X component** | 183.89*cos(${AoA}) |
| **Velocity – Y component** | 183.89*sin(${AoA}) |
| **Static pressure (p)** | 0.0 Pa |
| **Turbulent Viscosity Ratio** | 0.2105 |

| Initialization and Numerical Control | |
|---|---|
| **Parameter** | **Value / Choice** |
| **Initialization** | Grid Sequencing Initialization (GSI) |
| **CFL number** | Min 0.5; Initial 5; Max. 50 |
| **Linear solver** | Algebraic Multigrid (AMG) |
| **AMG Convergence Tolerance** | 0.001 |
| **URF (Turbulence)** | 0.5 |
| **URF (Viscosity)** | 0.2 |
| **Boundary Conditions** | |
| **Parameter** | **Value / Choice** |
| **Mach (M)** | 0.85 |
| **Flow direction – X component** | cos(${AoA}) |
| **Flow direction – Y component** | sin(${AoA}) |
| **Static temperature (T)** | 116.48 K |
| **Static pressure (p)** | 0.0 Pa |
| **Turbulent Viscosity Ratio** | 0.2105 |

## 6. Results

This section presents the numerical results. First, the flow field is compared across the angle-of-attack (AoA) sweep. The alpha = 4.00 degree condition is then analyzed in detail to compare simulations with and without AMR. Finally, the aerodynamic coefficients are compared with wind-tunnel data and DPW-7 submissions [5,6,7,8,10,18].

### 6.1 Comparison Across Angles of Attack

Figure 1 shows Mach-number contours along the airfoil section for simulations performed without AMR across the angle-of-attack sweep.

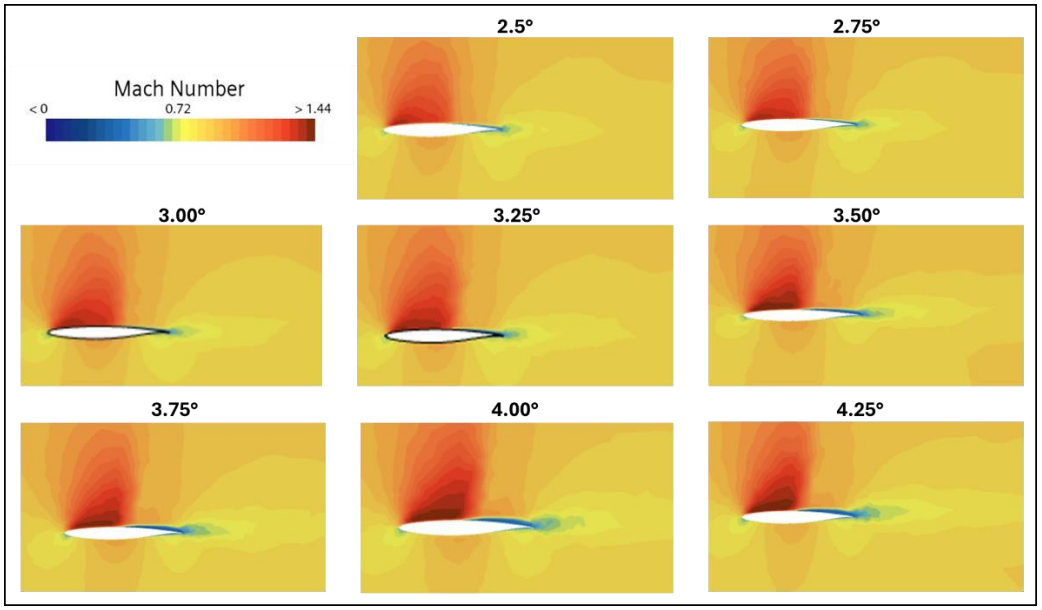



Figure 1 – Mach number contours for all angles of attack.

As AoA increases, the low-Mach-number region becomes more pronounced and moves upstream, indicating earlier boundary-layer separation under an increasingly adverse pressure gradient. At the highest angles, the low-speed region thickens and extends downstream, consistent with stronger shock-induced separation. This trend is especially visible at alpha = 4.25 degrees, where the separated region is well developed, and the solution approaches the nonlinear aerodynamic behavior associated with pitch break [4,11,12].

Figure 2 shows total pressure coefficient contours for the same cases. At lower angles of attack, the boundary layer remains mostly attached, and the wake is narrow with relatively small total pressure losses. At higher angles, stronger shock-boundary-layer interaction and larger separated regions produce a thicker and more irregular wake. The increased total-pressure loss is visible in the wake at alpha = 4.00 degrees and alpha = 4.25 degrees.

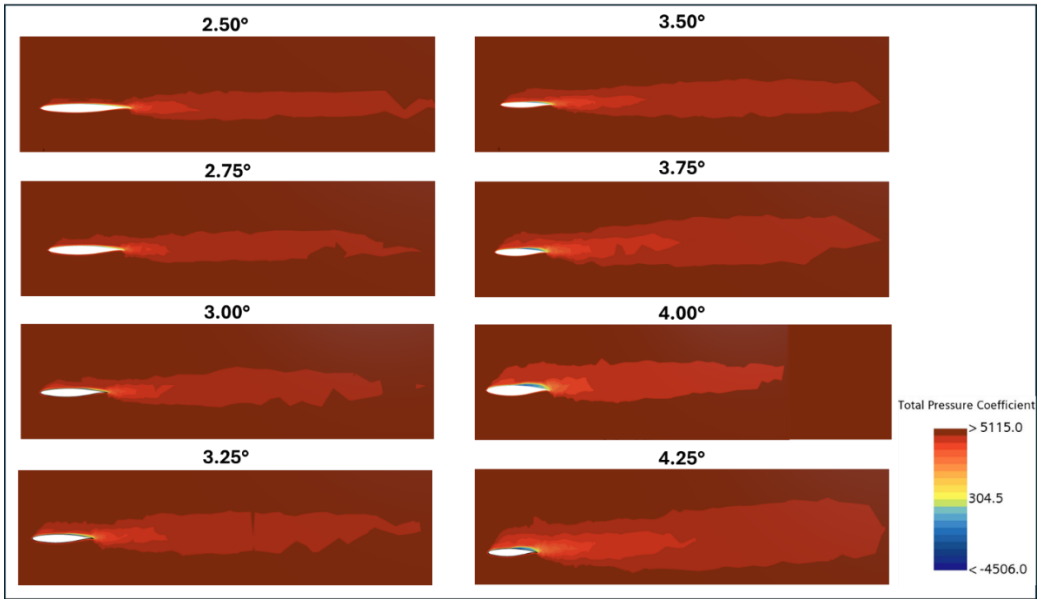



Figure 2 – Total pressure coefficient contours for all angles of attack.

These flow features directly affect the integral aerodynamic coefficients. Pitching moment is especially sensitive because shock motion and separation change the chordwise pressure distribution and shift

the aerodynamic loading. It is therefore necessary to assess whether the simulations reproduce the pitch-break trend in addition to the global lift and drag behavior [4,11,12].

### 6.2 AoA of 4.00 degrees with and without AMR

The AoA = 4.00-degree condition was selected for detailed analysis because it represents a demanding transonic regime with pronounced shock waves and strong pressure gradients. This condition was also selected in DPW-7 for detailed pressure-coefficient comparisons along the wing chord at several spanwise stations. It is therefore a useful case for assessing both the reduced mesh and the AMR strategy against reference data [1,7,18].

Figure 3 shows the baseline surface mesh on the fuselage and wing in the upper panels and the corresponding meshes after AMR in the lower panels. The refinement is concentrated primarily in the wake regions, where the vorticity magnitude is high and the flow gradients are stronger.

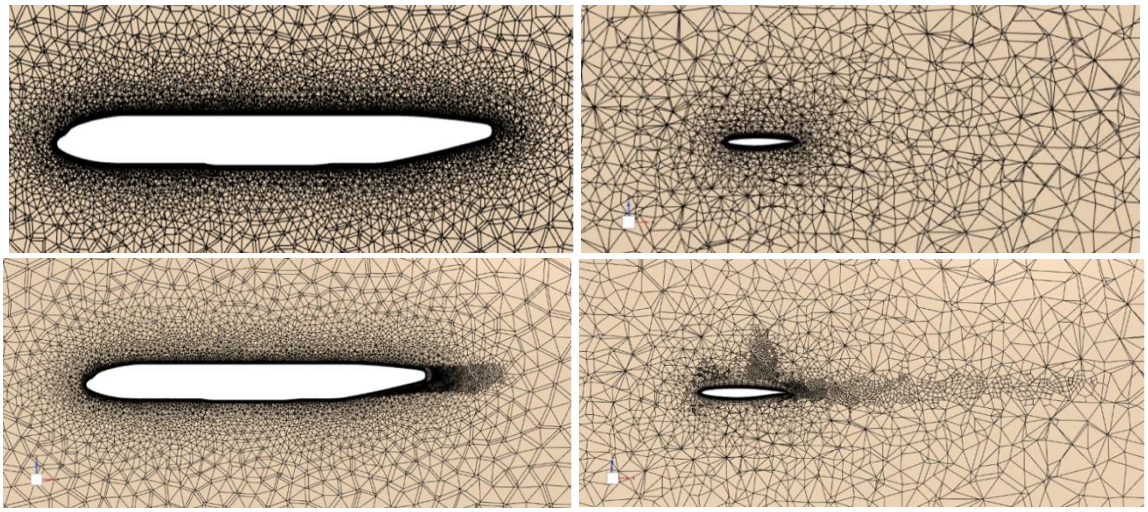


Figure 3 – Surface mesh comparison before and after adaptive mesh refinement. The upper panels show the baseline meshes on the fuselage (left) and wing (right), while the lower panels show the corresponding meshes after AMR.

Despite the targeted refinement produced by AMR, the improvement in the aerodynamic coefficients was limited. The AMR mesh slightly reduced the drag coefficient, suggesting some improvement in wake and recirculation resolution. However, lift and pitching moment moved farther from the wind-tunnel values, as shown in Table 2.

Table 2 – Aerodynamic coefficients with and without AMR compared to wind-tunnel data (AoA = 4.0 degrees).

| | **Without AMR** | **With AMR** | **Wind Tunnel** |
|---|---|---|---|
| $C_D$ (Drag) | 0.055 | 0.053 | 0.046 |
| $C_L$ (Lift) | 0.628 | 0.590 | 0.655 |
| $C_M$ (Pitching moment) | -0.068 | -0.039 | -0.077 |

These results indicate that the level, extent, and criterion of the localized refinement were not sufficient to produce a consistent improvement in overall accuracy [20,21,22,23,24].

The qualitative flow structure remained broadly similar between the baseline and AMR configurations. Figure 4 shows comparable patterns in total pressure coefficient, Mach number and wall shear stress for both meshes. Figure 5 shows that the pressure-coefficient distributions along the chord have similar shapes and nearly identical shock locations. The localized refinement therefore preserved the global flow pattern but did not materially change the pressure loading that controls the pitching moment.

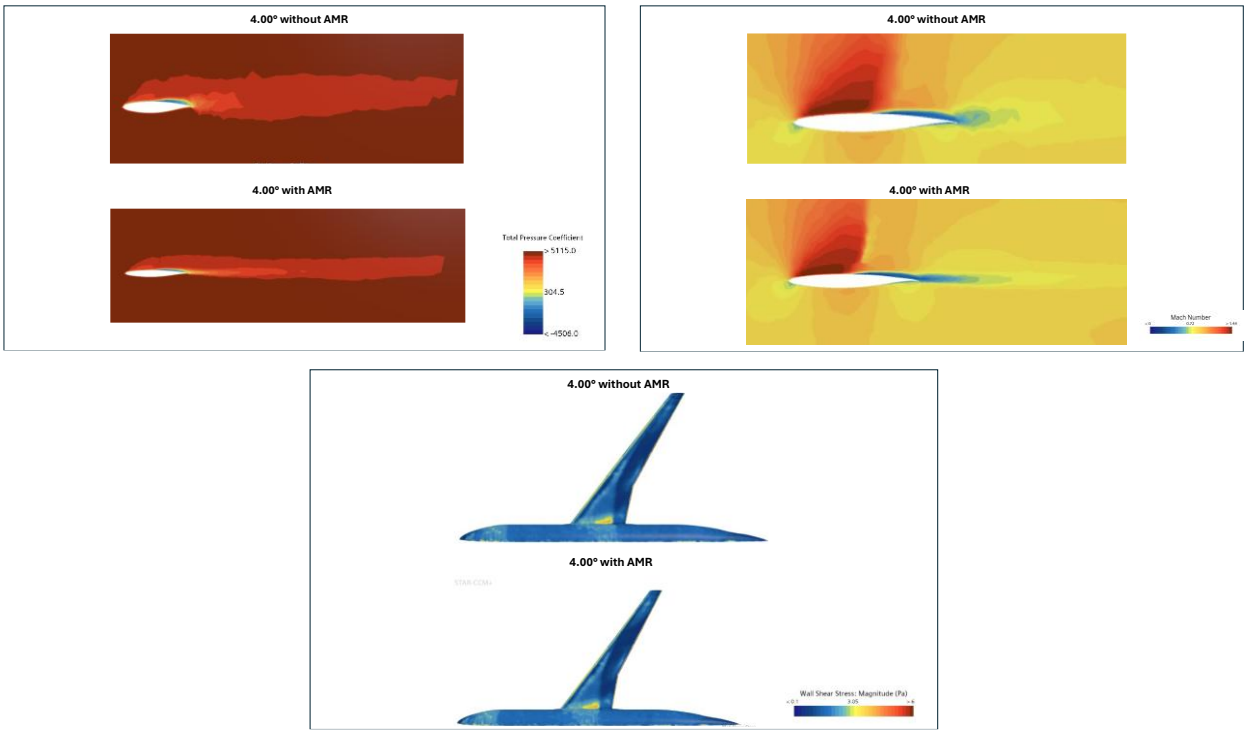



Figure 4 – Baseline and AMR total-pressure coefficient (top left), Mach number at the wing section (top right), and wall shear stress (bottom).

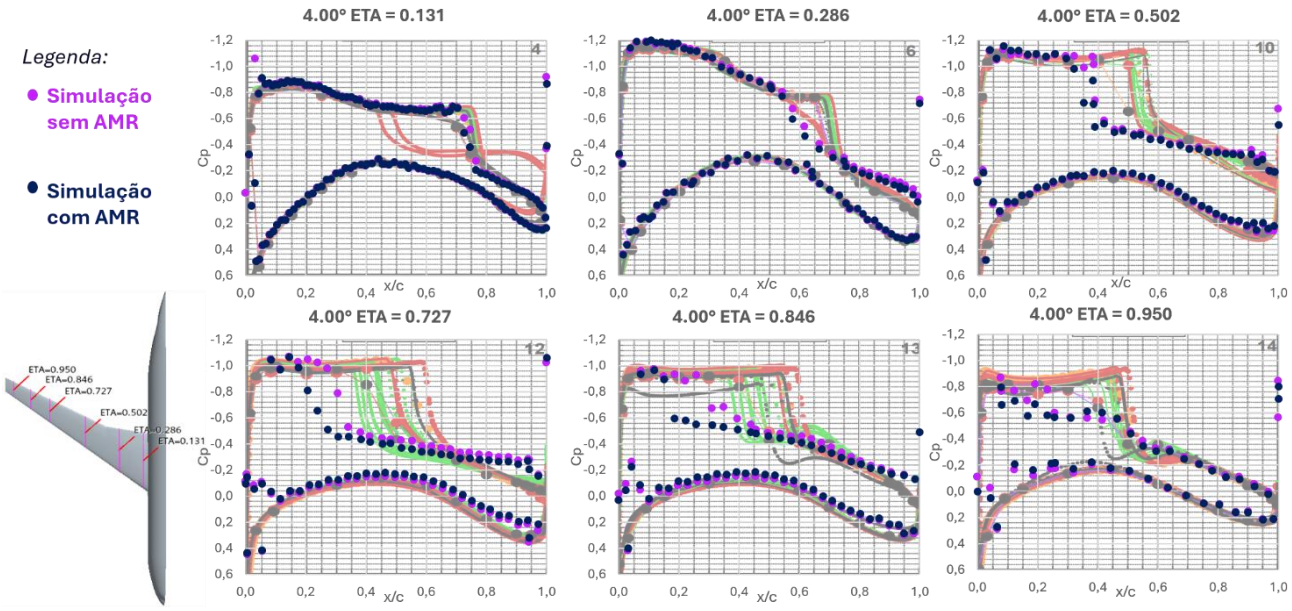



Figure 5 – Baseline and AMR pressure-coefficient distributions along the chord.

For AMR to become more effective in this problem, additional studies should test refinement variables and thresholds that better target the mechanisms controlling pitching moment, including shock position, shock-foot structure, near-wall resolution and chordwise pressure gradients [20,21,22,23,24].

### 6.3 Comparison With Wind-Tunnel Data and DPW-7 Submissions

To assess the numerical results, the simulations are compared with Embraer reference results available

to the authors, solutions submitted by other DPW-7 participants, and experimental wind-tunnel data from the European Transonic Wind Tunnel. The comparison focuses on the accuracy of the aerodynamic coefficients and on the likely physical or numerical sources of discrepancy [5,6,7,8,10,18]. Figure 6 shows the lift coefficient as a function of angle of attack for Case 2a, together with DPW-7 submissions, the Embraer reference simulation and the European Transonic Wind Tunnel data [5,6,7,8,10,18]. At lower angles of attack, the present coarse-mesh results slightly overpredict $C_L$, indicating that the initial lift buildup is reasonably captured. As the angle of attack increases, the predicted $C_L$ growth rate becomes smaller than the experimental trend, leading to lower lift at higher incidence. This behavior is consistent with the limited mesh resolution and turbulence-model sensitivity in the separated transonic regime. The medium-mesh results fall within the DPW-7 envelope and show a steeper local lift slope, closer to the experimental trend [5,6,8,10,18].

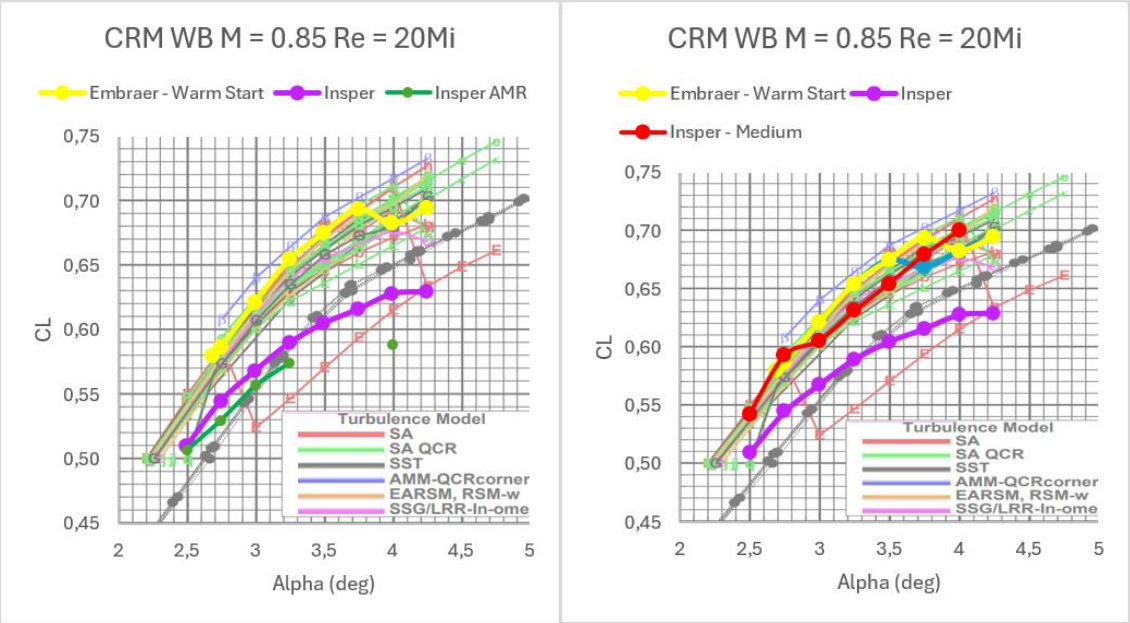



Figure 6 – Lift coefficient as a function of angle of attack for DPW-7 Case 2a: comparison between the present coarse-mesh results, medium-mesh results, Embraer reference simulation, DPW-7 submissions and European Transonic Wind Tunnel data.

Figure 7 shows the relationship between lift coefficient and pitching-moment coefficient and highlights the pitch-break behavior [5,6,7,8,10,18]. The present coarse-mesh curve captures the qualitative nonlinear trend of the experimental $C_m$ response, including the change in slope around $C_L \approx 0.6$ to 0.7. However, the predicted pitch-break onset occurs between AoA values of 3.00 and 3.25 degrees, slightly earlier than the experimental range of approximately 3.25 to 3.75 degrees. The medium-mesh results lie closer to the Embraer reference and shift the predicted moment level relative to the coarse-mesh curve, indicating that the chordwise pressure distribution is better resolved at higher mesh resolution [5,6,8,10,18].

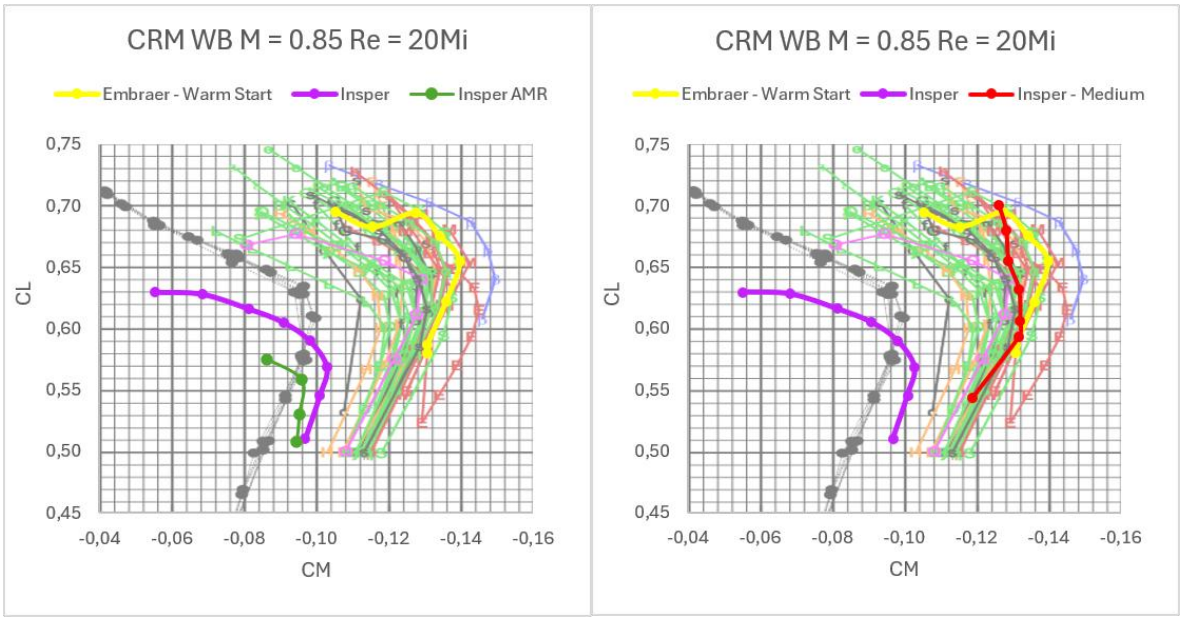



Figure 7 – Lift coefficient as a function of pitching-moment coefficient for DPW-7 Case 2a: comparison between the present coarse-mesh results, medium-mesh results, Embraer reference simulation, DPW-7 submissions and European Transonic Wind Tunnel data.

Figure 8 shows the lift–drag polar for Case 2a [5,6,7,8,10,18]. The coarse-mesh results reproduce the experimental polar shape but are shifted toward higher CD values, indicating drag overprediction. This offset suggests limited near-wall and wake resolution. The medium-mesh results move closer to the experimental data and Embraer reference simulation, confirming that the drag discrepancy is mainly caused by mesh resolution. Remaining differences are consistent with the fully turbulent RANS formulation used in this study [16].

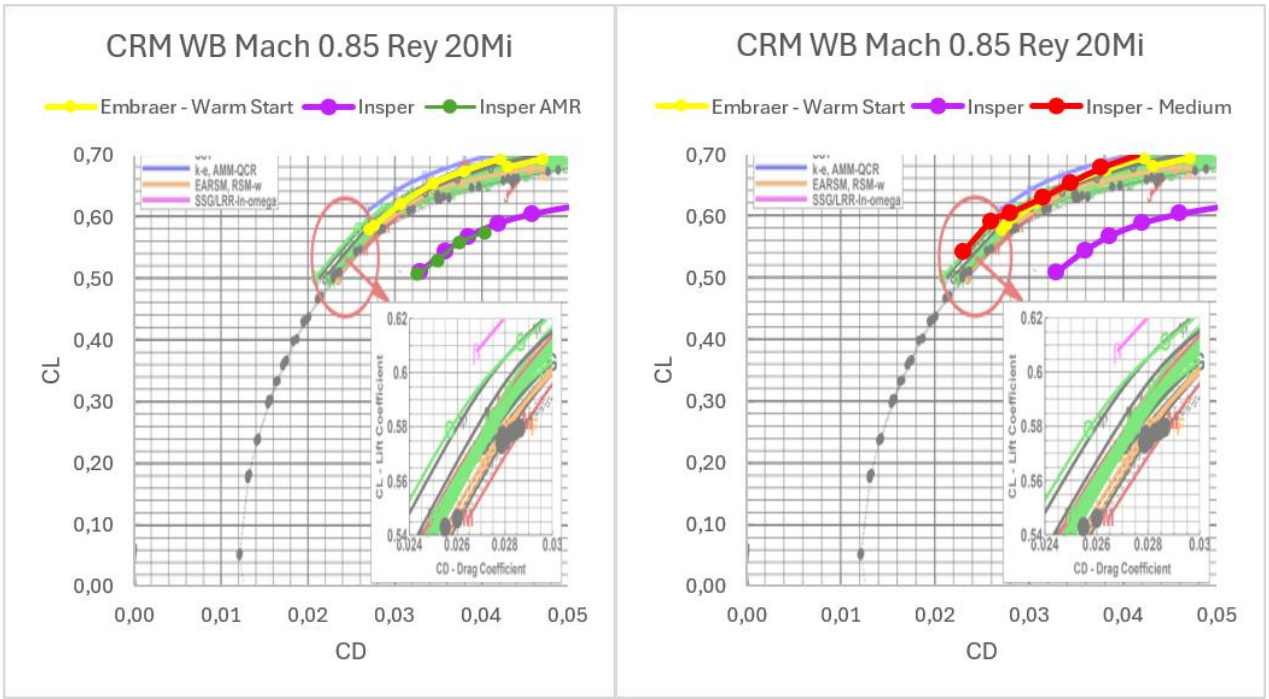



Figure 8 – Lift–drag polar for DPW-7 Case 2a: comparison between the present coarse-mesh results, medium-mesh results, Embraer reference simulation, DPW-7 submissions and European Transonic Wind Tunnel data.

Across the coefficient comparisons, the reduced-mesh simulation captures the main aerodynamic trends of the CRM wing-body configuration at a substantially lower cell count than the medium-resolution DPW-7 reference grids. The medium-mesh results confirm the sensitivity of lift slope, drag level, and pitching moment to mesh resolution. The results therefore support the use of low-cost meshes for exploratory studies, while showing that quantitatively reliable pitching-moment prediction in this transonic regime requires more targeted refinement [5,6,8,10,18].

## 7. Conclusion

This work reproduced DPW-7 Case 2a for the NASA Common Research Model wing-body configuration at Mach 0.85 and Reynolds number 20 million, with emphasis on the trade-off between computational cost and aerodynamic fidelity in transonic pitching-moment prediction [1,7,18]. A reduced baseline mesh with approximately 4.7 million cells was used to perform the complete angle-of-attack sweep and to assess whether a low-cost numerical setup could recover the main aerodynamic trends reported in the workshop data.

The reduced mesh captured the overall lift, drag, and pitching-moment behavior of the configuration, including the qualitative nonlinear trend associated with pitch break. However, the results also showed clear limitations. The lift slope became less accurate at higher angles of attack, the drag level was systematically overpredicted, and the predicted pitch-break onset occurred earlier than in the experimental data. These discrepancies are consistent with insufficient resolution of shock-induced separation, near-wall gradients and wake development, which are critical for moment-sensitive transonic flows [5,6,8,10,18].

The comparison with the medium-mesh simulations confirmed that mesh resolution is a dominant factor in the observed discrepancies. The medium-mesh results moved closer to the experimental data and to the Embraer reference solution, especially in the lift curve and drag polar. This indicates that the main numerical setup was able to reproduce the expected aerodynamic behavior, but that the coarse mesh did not provide enough spatial resolution to capture all pressure-loading features required for accurate pitching-moment prediction [5,6,8,10,18].

The vorticity-based adaptive mesh refinement test at AoA = 4.00 degrees produced localized refinement mainly in wake regions and preserved the qualitative flow structure of the baseline solution. Nevertheless, it did not improve the pitching-moment prediction and led to only limited changes in the integral aerodynamic coefficients. This result indicates that vorticity magnitude alone is not an adequate refinement indicator for this case, because the pitching moment is controlled primarily by the chordwise pressure distribution, shock position and shock-induced separation over the wing [20,21,22,23,24].

Overall, the study shows that reduced meshes can be useful for exploratory transonic simulations and for identifying global aerodynamic trends at moderate computational cost. However, they are not sufficient for high-fidelity prediction of pitching moment and pitch-break onset without carefully targeted refinement. Future work should therefore investigate refinement indicators more directly connected to the relevant physics, including shock sensors, pressure-gradient-based criteria, separation indicators, and adjoint-based mesh adaptation [20,21,22,23,24]. Future work could also assess unsteady or hybrid RANS/LES approaches for separated transonic regions when higher-fidelity flow resolution is required [17]. Additional mesh-convergence studies and improved near-wall resolution are also required to establish a more reliable balance between computational cost and predictive accuracy for transonic aerodynamic applications.

## 8. Acknowledgments

The authors acknowledge the National Laboratory for Scientific Computing (LNCC/MCTI, Brazil) for providing HPC resources on the SDumont supercomputer, which contributed to the results reported in this paper. Available at: http://sdumont.lncc.br.

## 9. Contact Author Email Address

The contact author email address is: gusribolla@gmail.com

## 10. Copyright Statement

The authors confirm that they, and/or their company or organization, hold copyright on all of the original

material included in this paper. The authors also confirm that they have obtained permission, from the copyright holder of any third party material included in this paper, to publish it as part of their paper. The authors confirm that they give permission, or have obtained permission from the copyright holder of this paper, for the publication and distribution of this paper as part of the ICAS proceedings or as individual off-prints from the proceedings.

## References

[1] American Institute of Aeronautics and Astronautics. 7th AIAA CFD Drag Prediction Workshop (DPW-7). Chicago, IL, 25–26 June 2022. https://www.aiaa-dpw.org/Workshop7/workshop7.html, accessed 10 September 2025.
[2] American Institute of Aeronautics and Astronautics. CFD Drag Prediction Workshop VII (DPW-7): expanding the envelope. AIAA, 2022. https://www.aiaa.org/docs/default-source/default-document-library/dpw-vii---expanding-the-envelope.pdf, accessed 10 September 2025.
[3] NASA Langley Research Center. DPW7 grids and files: JAXA_Grids.REV00. 2022. https://dpw.larc.nasa.gov/DPW7/JAXA_Grids.REV00/, accessed 20 September 2025.
[4] Anderson JD. *Fundamentals of aerodynamics.* 5th edition, McGraw-Hill, 2010.
[5] Keye S, Brodersen O and Melber-Wilkending S. Summary of DLR results from the seventh AIAA Drag Prediction Workshop. *Proc 34th Congress of the International Council of the Aeronautical Sciences (ICAS 2024)*, Florence, Italy, paper ICAS2024_0116, pp 3992–4008, 2024.
[6] Eliasson P, Peng SH and Prachař A. Influence of turbulence modelling and grid resolution in computations of the DPW7 CRM configuration. *Proc AIAA AVIATION 2023 Forum*, San Diego, CA, AIAA Paper 2023-4091, 2023. https://doi.org/10.2514/6.2023-4091.
[7] Rivers MB, Quest J and Rudnik R. Comparison of the NASA Common Research Model European Transonic Wind Tunnel test data to NASA test data. *Proc 53rd AIAA Aerospace Sciences Meeting*, Kissimmee, FL, AIAA Paper 2015-1093, 2015. https://doi.org/10.2514/6.2015-1093.
[8] Hue D, Sartor F, Petropoulos I and Fournis C. DPW-7: steady and unsteady computations of the Common Research Model at different Reynolds numbers. *Journal of Aircraft*, Vol. 60, No. 6, pp 1857–1871, 2023. https://doi.org/10.2514/1.C037231.
[9] National Aeronautics and Space Administration. NASA Common Research Model: geometry and test data. NASA Langley Research Center, 2010. https://commonresearchmodel.larc.nasa.gov/, accessed 22 September 2025.
[10] Plante F. DPW7 results from CHAMPS, including global stability analyses. *Proc AIAA AVIATION 2023 Forum*, San Diego, CA, AIAA Paper 2023-3399, 2023. https://doi.org/10.2514/6.2023-3399.
[11] Raymer DP. *Aircraft design: a conceptual approach.* 6th edition, American Institute of Aeronautics and Astronautics, Reston, VA, 2018. https://doi.org/10.2514/4.104909.
[12] Sadraey MH. *Aircraft design: a systems engineering approach.* 1st edition, John Wiley & Sons, Chichester, 2013. https://doi.org/10.1002/9781118352700.
[13] Siemens Digital Industries Software. *Simcenter STAR-CCM+ user guide.* Siemens, 2025.
[14] Siemens Digital Industries Software. *Best practices: external aerodynamics for aerospace applications.* Siemens, Plano, TX, 2020.
[15] Siemens Digital Industries Software. *Simcenter STAR-CCM+ recommended physics/solver setup: external aerodynamics for aerospace applications.* Siemens, 2023.
[16] Spalart PR and Allmaras SR. A one-equation turbulence model for aerodynamic flows. *Proc 30th Aerospace Sciences Meeting and Exhibit*, Reno, NV, AIAA Paper 92-0439, 1992. https://doi.org/10.2514/6.1992-439.
[17] Spalart PR, Deck S, Shur ML, Squires KD, Strelets MKh and Travin A. A new version of detached-eddy simulation, resistant to ambiguous grid densities. *Theoretical and Computational Fluid Dynamics*, Vol. 20, No. 3, pp 181–195, 2006. https://doi.org/10.1007/s00162-006-0015-0.
[18] Tinoco EN. Summary data from the seventh AIAA CFD Drag Prediction Workshop. *Proc AIAA AVIATION 2023 Forum*, San Diego, CA, AIAA Paper 2023-3492, 2023. https://doi.org/10.2514/6.2023-3492.
[19] Vassberg JC, DeHaan MA, Rivers SM and Wahls RA. Development of a Common Research Model for applied CFD validation studies. *Proc 26th AIAA Applied Aerodynamics Conference*, Honolulu, HI, AIAA Paper 2008-6919, 2008. https://doi.org/10.2514/6.2008-6919.
[20] Nemec M, Aftosmis MJ and Wintzer M. Adjoint-based adaptive mesh refinement for complex geometries. *Proc 46th AIAA Aerospace Sciences Meeting and Exhibit*, Reno, NV, AIAA Paper 2008-0725, 2008. https://doi.org/10.2514/6.2008-725.
[21] Balan A, Park MA and Anderson WK. Adjoint-based anisotropic mesh adaptation for a stabilized finite-element flow

solver. *Proc AIAA AVIATION 2019 Forum*, Dallas, TX, AIAA Paper 2019-2949, 2019. https://doi.org/10.2514/6.2019-2949.
[22] Alauzet F and Frazza L. 3D RANS anisotropic mesh adaptation on the high-lift version of NASA's Common Research Model (HL-CRM). *Proc AIAA AVIATION 2019 Forum*, Dallas, TX, AIAA Paper 2019-2947, 2019. https://doi.org/10.2514/6.2019-2947.
[23] Fidkowski KJ and Darmofal DL. Review of output-based error estimation and mesh adaptation in computational fluid dynamics. *AIAA Journal*, Vol. 49, No. 4, pp 673–694, 2011. https://doi.org/10.2514/1.J050073.
[24] NASA Langley Research Center. Adjoint-based adaptation applied to AIAA DPW II wing-body. FUN3D Example 39. https://fun3d.larc.nasa.gov/example-39.html, accessed 7 November 2025.